Delft University of Technology

Fault Location Algorithm for Multi-Terminal Radial Medium Voltage DC Microgrid

Nougain, Vaibhav; Mishra, Sukumar; Nag, Soumya Shubhra; Lekic, Aleksandra

Important note
To cite this publication, please use the final published version (if applicable).
Please check the document version above.

Fault Location Algorithm for Multi-Terminal Radial Medium Voltage DC Microgrid

Vaibhav Nougain [ID], Sukumar Mishra [ID], *Senior Member, IEEE*, Soumya Shubhra Nag [ID], *Member, IEEE*, and Aleksandra Lekić [ID], *Senior Member, IEEE*

Abstract—Accurately locating the fault helps in the rapid restoration of the isolated line back into the system. This article proposes a novel communication-based multi-terminal method to locate the fault in a radial medium voltage DC (MVDC) microgrid. A time-domain based algorithm is proposed which applies to an MVDC system with different possible combinations of lines and cables. Terminal measurements of voltages and currents, voltages across current limiting reactor (CLR), and node currents are used to propose a flexible online fault location method. Based on the availability of communication and sensors, different terminals can be used to increase the reliability of the proposed fault location method. This method is robust to variations of key implementation parameters like type of faults, fault resistance, fault location, sampling frequency, white Gaussian noise (WGN) in measurement, and different line/cable combinations. Further, the fault location calculation is analyzed with parameter variation. PSCAD/EMTDC based electromagnetic transient simulations are used to validate the performance of the algorithm.

Index Terms—Power system protection, microgrids, power distribution faults, fault location.

I. INTRODUCTION

MVDC microgrid serves the requirement of supplying the shipping service and propulsion loads in shipboard electrical systems [1], [2], [3], onboard DC marine vessels [4], [5], and remote area mine sites [6]. This is a result of various advantages [7] including (i) lesser losses, (ii) lesser complexity with a lesser number of conversion stages in the system, (iii) relaxed synchronization requirements, and (iv) easy integration of multiple energy storage systems. Such multi-terminal MVDC microgrids, when subjected to a fault contingency experience a high rate of rise of current due to discharging converter capacitor [1]. The interfacing converter is prone to get damaged in case of improper control logic [7]. Even if the control is proper,

the converter control is bypassed to limit the current [8] affecting the power transfer in the system. Either way, there is an indispensable requirement for a fast, selective, and reliable protection approach that ensures continuous operation of power transfer even under a fault [1]. Protection has two broad challenges, (i) fault identification and (ii) fault location. Identifying the fault helps in the isolation of the faulty line and accurately locating the DC fault ensures rapid restoration of the isolated faulty line into the DC system.

Focussing on the aspect of DC fault location, the literature has mainly covered low voltage DC (LVDC) and high voltage DC (HVDC) fault location. Generally, LVDC systems have the attribute of short lines (up to 1 km) for distribution and a low value of fault resistance (up to 5 Ω) [9], [10], [11], [12], [13], [14], [15], [16], [17]. Since the cost can be a constraint for such a system, single terminal methods are suitable for fault location in LVDC systems [9], [10], [11], [12], [13], [14], [15], [16], [17]. Single terminal methods do not require communication i.e., other terminal data to locate the fault. However, the accuracy of single terminal fault location methods has inherent dependence on fault resistance whereas double terminal (or multi-terminal) methods eliminate the dependence [9]. This means double terminal (or multi-terminal) methods are accurate even for high resistance faults. They come with the inherent problem of communication complexity and extra cost [12]. Discussing single terminal fault location methods, the authors in [14], [15], [16] use a probe power unit (PPU) as an active external injection unit. The method in [14] neglects the damping coefficient in the second order RLC discharging circuit, taking the damped frequency equal to the natural frequency. This results in a deviation in the accuracy of fault distance. The method in [15] uses a least square algorithm to evaluate the damping i.e., attenuation constant. However, when the attenuation constant is high, the accuracy of the method is jeopardized. Authors in [16] use modified PPU to calculate the high value of attenuation constant and thereby, evaluate fault distance with higher accuracy in comparison to [14], [15], [16]. The authors in [13] use a fault location module, consisting of an inductor, two switches, and two thyristors to achieve an accuracy of 98.4% for low resistance faults in the LVDC system. However, the method in [13] is prone to be affected by WGN in measurement as it uses the differential term (*di/dt*) in the analysis of fault location. Authors in [17] propose an iterative method to evaluate fault location for pole-to-ground (PTG) faults without any external modification. However, this method has a dead zone for faults closer to the bus and for

Fault Location Methods	Method Type/Communication needed?	External modifications	Limitations
[11]	Time-domain LVDC/No	multiple capacitive earthing method	limited to low fault resistance and homogeneous lines
[13]	Time-domain LVDC/Yes	fault location module	limited to low fault resistance and homogeneous lines
[14]-[16]	Time-domain LVDC/No	probe power unit	limited to low fault resistance and homogeneous lines
[17]	Time-domain LVDC/No	No	limited to homogeneous lines
[20]	Time-domain HVDC/Yes	current limiting reactor	limited to homogeneous lines
[21]	Travelling-wave non-homogeneous HVDC/Yes	current limiting reactor	limited to fault resistance, $R_f < 100\,\Omega$
[24]	Time-domain HVDC/Yes	current limiting reactor	limited to homogeneous lines
[Proposed method]	Time-domain non-homogeneous MVDC/Yes	current limiting reactor	sensitive to parameter variation (much like other time-domain methods)

pole-to-pole (PTP) faults. The method in [9] proposes the use of CLR in the single terminal fault location method. Based on the ratio of transient voltages (ROTV), the analysis is robust and mathematically convincing. The authors in [10] use an improved solid-state circuit breaker (SSCB) to propose a curve-fitting method. However, the parameter extraction method presents low accuracy when the fault occurs close to the bus. The authors in [11] use multiple capacitance earthing as external modifications. However, the method is prone to WGN in measurement as it uses differential terms (di/dt and dv/dt) in the analysis of fault location.

Generally, HVDC systems have long lines for transmission and the possibility of high fault resistance [19], [20]. As a result, double-terminal (or multi-terminal) methods are suitable for fault location in such a system [20], [21], [22], [23], [24]. Long transmission lines come with the additional problem of communication delay, which needs consideration. Discussing double terminal methods, the authors in [20] use time-domain-based simplified R-L representation of transmission lines [18], [19] to model overhead lines (OHLs) for fault location in HVDC systems. However, the mathematical scope of the work limits the application of the methods to homogeneous lines or cables. The authors in [21], [22] address the problem of fault location for non-homogeneous DC transmission comprising segments of UGC and segments of OHL. The authors in [21] use the traveling wave-based double terminal method to detect the surge arrival time accurately. The method is limited to a fault resistance of $100\,\Omega$ and requires a high sampling frequency. The authors in [22] propose a traveling wave type method using continuous wavelet transform applied to a series of line current measurements. The method addresses the problem of [21]. However, multiple distributed current sensors put the viability of the scheme to question. The authors in [24] propose fault location using synchronized currents of the conductors and sheaths of cables. The analysis in [24] is focused on pole-to-pole faults in underground transmission cables (where overhead lines are not included in the studies). The authors in [24] also successfully introduce a generalized fault location analysis for a bigger DC system. The thorough analysis does not use voltage measurements to evaluate fault location. This reduces the cost of the implementation of the method. However, the complexity of the computation of the algorithm is higher due to fewer measured quantities (e.g., evaluation of Z_{seen}). Additionally, the method does not exclusively consider a non-homogeneous transmission for fault

location, which limits the application of the method to homogeneous transmission cables only. The broad comparison of exisiting schemes in literature and the proposed method is shown in Table I.

MVDC systems have the attribute of short lines for distribution and have the possibility of a high value of fault resistance [1], [7]. This makes double-terminal (or multi-terminal) methods more suitable than single-terminal methods for accurate fault location. Additionally, due to shorter lines, communication delay in the MVDC system is not a concern [6]. To the best of the authors' knowledge, the literature has not covered the application of time-domain-based methods for non-homogeneous lines or cables in MVDC systems. This results from limited mathematical exploration in the area of time-domain-based fault location methods for MVDC systems. This work proposes a novel time-domain-based fault location algorithm for multi-terminal radial MVDC microgrids. The proposed work has the following attributes:

- Unlike single terminal methods [9], [10], [11], [12], [13], [14], [15], [16], [17], the proposed work is accurate even for high resistance faults.
- Unlike time-domain-based double terminal methods [18], [19], [20], the method is flexible for systems with either homogeneous or non-homogeneous combinations of cables and lines for distribution.
- Unlike traveling wave-based double-terminal methods [21], [22], the proposed work requires a sampling frequency as low as 5 kHz (see Section V(D)) and is fairly accurate for high resistance faults.
- The proposed work generalizes the analysis for a larger MVDC system with k nodes and p buses for broader application. Based on the availability of communication at different terminals, the method can be applied to increase the reliability of fault location.
- The method is robust to variation of key parameters like type of faults, fault resistance, fault location, and white Gaussian noise in the measurement.

The rest of the proposed work is organized as follows. Section II introduces the test system configuration and Section III explains the differential fault identification method. Section IV presents the fault location algorithm whereas Section V gives the implementation of the proposed method. Section VI validates the proposed fault location algorithm whereas Section VII concludes the work.
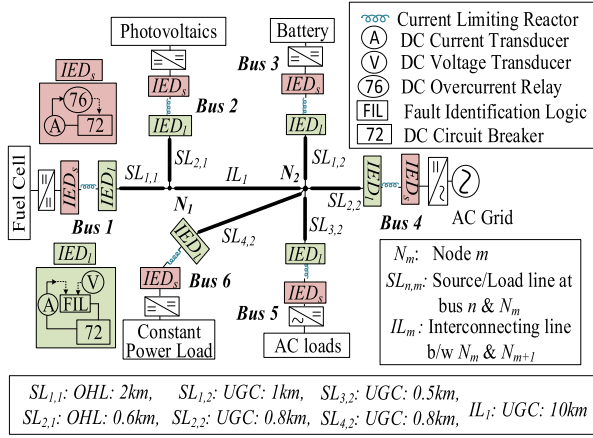
Fig. 1.   Medium voltage DC test system.

II. TEST SYSTEM CONFIGURATION

A multi-terminal MVDC microgrid operating at ± 2 kV formed by a radial configuration of 6 buses [24] is used as a test system (see Fig. 1). Bus 1 has a fuel cell, whereas bus 2 has a photovoltaic system interfaced to the system with a boost DC/DC converter. Bus 3 has an energy storage system (ESS) battery interfaced with a bidirectional DC/DC converter. Bus 4 has an AC utility grid connected to the DC system with a voltage source converter (VSC). Bus 5 has grid forming VSC interfaced AC loads, whereas bus 6 has buck DC/DC converter interfaced constant power loads (CPL) [1], [7].

A bipolar line configuration with a frequency-dependent transmission model (FDTL) for UGC and OHL is considered for the system. The UGC is modeled as single-core 280 mm^2 cables with copper conductor, XLPE insulation (2.8 mm thick), and PVC sheathing (2.5 mm thick), whereas the OHL is modeled as ACSR based stranded conductor with an outer radius of 0.02 m and strand radius of 0.003 m. The grounding capacitance for UGC and OHL is within 0.5 μF/km and 0.01 μF/km, respectively, while the equivalent DC capacitors of the converters are around 1–10 mF. Hence, the fault contribution from the grounding capacitance of cables and lines can be ignored for short to medium lengths [1]. As a result, the R-L representation of UGC and OHL is used for the fault location analysis. The grounding scheme considered is TN-S which provides mid-point grounding at each converter terminal. The fault contingencies considered in the test system are of different types i.e., PTP, positive-pole to ground (P-PTG), and negative-pole to ground (N-PTG). The sources and loads in the setup are protected using intelligent electronic devices, IED_s which is a combination of DC current transducer, DC overcurrent relay, and DC circuit breakers as shown in Fig. 1. The cables and lines in the system are protected with IED_l using a differential current relay (DCR) as the fault identification scheme [1]. CLRs are used in Fig. 1 to limit the current rise rate during a fault contingency. The CLRs are placed between every IED_s and IED_l. Buses connected to their respective nodes, N_1 & N_2 are used to divide the system shown in Fig. 1 into two parts. Buses 3–6 of the system act as buses 1–4 for node, N_2 whereas buses 1–2 of the system act

as buses 1–2 for node, N_1. As a result of which, $SL_{1,2}$ means source line connected at bus 1 of node 2 (or bus 3 of the system), $SL_{2,2}$ means source line connected at bus 2 of node 2 (or bus 4 of the system) and so on. The measurement points for each bus are DC output voltage, voltage after CLR, current through CLRs and adjacent node current (in the case of a multi-terminal system). Node current is important for fault identification using DCR. In case, the node current measurements are unavailable, a localized voltage-based fault identification method [1] can be used along with the DCR.

III. FAULT IDENTIFICATION ALGORITHM

The fault is identified and classified into different types i.e., PTP, P-PTG and N-PTG at either $SL_{j,i}$ or IL_i. DCR uses bus and node current values to make a trip decision for a fault. To identify and classify faults at $SL_{j,i}$, the trip condition is given by (1a) and (1b).

$$\begin{cases} i_{Bj,i^+}(k) = \left| i_{j,i^+}(k) - i_{Ni^+}(k) \right| > I_{set} & \text{(1a)} \\ i_{Bj,i^-}(k) = \left| i_{j,i^-}(k) - i_{Ni^-}(k) \right| > I_{set} & \text{(1b)} \end{cases}$$

where $i_{j,i^+}(k)$ and $i_{j,i^-}(k)$ give the positive and negative pole currents from bus j with closest node i. $i_{Ni^+}(k)$ and $i_{Ni^-}(k)$ give the positive and negative pole currents at node i into the fault. The differential current feeds the fault and increases above a certain threshold, I_{set}. To identify and classify faults at IL_i, the trip condition is given by (2a) and (2b).

$$\begin{cases} i_{Nj,i^+}(k) = \left| i_{Ni^+}(k) - i_{N(i+1)^+}(k) \right| > I_{set} & \text{(2a)} \\ i_{Nj,i^-}(k) = \left| i_{Ni^-}(k) - i_{N(i+1)^-}(k) \right| > I_{set} & \text{(2b)} \end{cases}$$

where $i_{N(i+1)^+}(k)$ and $i_{N(i+1)^-}(k)$ give the positive and negative pole currents at node $(i+1)$ into the fault.

IV. FAULT LOCATION ALGORITHM

Once the fault is identified, the proposed fault location algorithm takes each segment with different values of R-L per unit. This allows locating fault for a system with any combination of lines or cables (varying from a homogeneous line or n-segment non-homogeneous lines i.e., a combination of OHL and UGC). Any terminal and faulty terminal can be used to calculate accurate fault location. The algorithm's reliability increases if the number of terminals is used to calculate location. The method is initially explained for a 2-node, 3-bus system (see Fig. 2). Further, a more complex system with 4 nodes, and 8 buses is analyzed for the fault location. Finally, the analysis is generalized for a k node, p bus system for wider applications to different MVDC systems.

A. Fault Location for a Three Bus System

A three bus MVDC system is shown in Fig. 2. Two nodes, N_1 and N_2 with three source/load lines (SL_1, SL_2 and SL_3) and one interconnecting line (IL_1) give four segments in the system. The analysis is elaborated considering node, N_1. The same analysis can be extended using node, N_2. A fault can occur at any of the
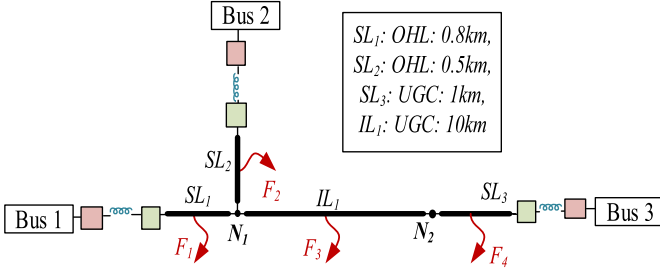
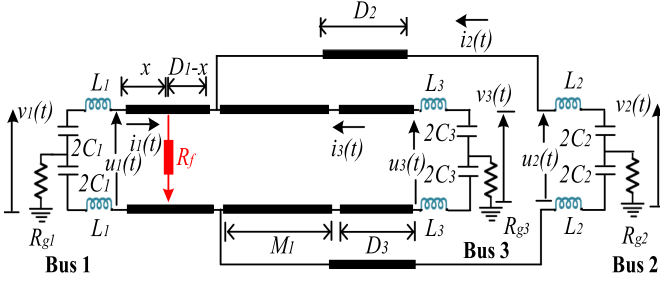Fig. 2. Generalised *2 node, 3 bus* MVDC system.

Fig. 3. Simplified *2 node, 3 bus* MVDC system.

segments as shown as F_1–F_4 in Fig. 2. The subsection covers a detailed derivation of fault location for different fault cases.

1) Fault at SL_1: If the fault is located at SL_1, given as F_1 in Fig. 2, the equivalent three-terminal system is given as shown in Fig. 3. Here $v_n(t)$ gives n^{th} DC link bus voltage, $u_n(t)$ gives the voltage after CLR and $i_n(t)$ gives current fed into the fault for *nth* bus. r_n is the resistance per unit length, l_n is the inductance per unit length and D_n is the total length of source/load line adjacent to *nth* bus. r_{Mm} is the resistance per unit length, l_{Mm} is the inductance per unit length and M_m is the total length of interconnecting line between *mth* to *(m+1)th* node. L is defined as value of CLR and R_f is defined as the fault resistance. Additionally, $x|_{B_n,N_m}$ is the fault distance calculated considering bus n, where $n \in \{1, 2, 3\}$. m is the node considered for reference along with bus n, where $m \in \{1, 2\}$.

Using Kirchhoff's Voltage Law (KVL) for a PTP fault at SL_1 (shown in Fig. 3), (3)–(5) are obtained for bus 1 to bus 3.

$$2r_1 x i_1(t) + 2l_1 x \frac{di_1(t)}{dt} + R_f \sum i(t) = u_1(t) \qquad (3)$$

$$\left. \begin{aligned} &2D_2 r_2 i_2(t) + 2l_2 D_2 \frac{di_2(t)}{dt} + 2(D_1 - x)r_1 \left[i_2(t) + i_3(t) \right] \\ &+ 2l_1 (D_1 - x) \left(\frac{di_2(t)}{dt} + \frac{di_3(t)}{dt} \right) + R_f \sum i(t) = u_2(t) \end{aligned} \right\}$$
$$(4)$$

$$\left. \begin{aligned} &2(D_3 r_3 + M_1 r_{M1}) i_3(t) + 2(l_3 D_3 + M_1 l_{M1}) \frac{di_3(t)}{dt} \\ &\qquad\qquad + 2(D_1 - x)r_1 \left[i_2(t) + i_3(t) \right] \\ &+ 2l_1 (D_1 - x) \left(\frac{di_2(t)}{dt} + \frac{di_3(t)}{dt} \right) + R_f \sum i(t) = u_3(t) \end{aligned} \right\}$$
$$(5)$$

Here $\sum i(t) = i_1(t) + i_2(t) + i_3(t)$. The current derivative terms can be obtained using the drop in voltage across the CLR, avoiding substitution errors due to differential calculations [9]. These
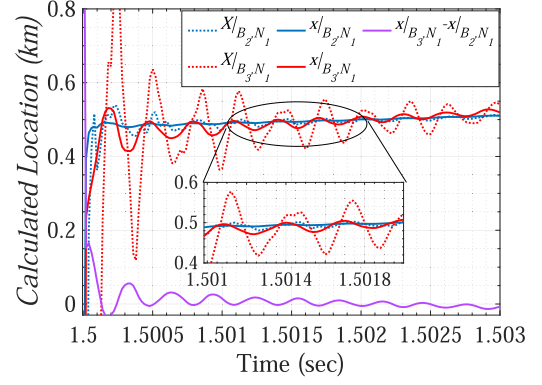
Fig. 4. Calculated location for a fault at SL_1.

terms are $\frac{di_1(t)}{dt} = \frac{v_1(t) - u_1(t)}{2L_1} = \frac{v_{L1}(t)}{2L_1}; \frac{di_2(t)}{dt} = \frac{v_2(t) - u_2(t)}{2L_2} = \frac{v_{L2}(t)}{2L_2}; \frac{di_3(t)}{dt} = \frac{v_3(t) - u_3(t)}{2L_3} = \frac{v_{L3}(t)}{2L_3}$. For the sake of simplicity in the analysis, $L_1 = L_2 = \cdots L_n$. Subtracting any two equations given in (3)–(5) negates the dependence of fault location on fault resistance, R_f. If the transition fault impedance has a resistive and an inductive component, (3)–(5) are given with an additional common inductive term $\left(l_f \frac{d[\sum i(t)]}{dt} \right)$. Since the term is common, it is canceled upon simplification. As a result, even if the transition fault impedance has an inductive component, the proposed fault location algorithm is still applicable without any changes. Rearranging (3) and (4) define the fault distance from bus 1 of node 1 considering bus 2 of node 1, given as (6).

$$\begin{aligned} &x|_{B_2,N_1} \\ &= \frac{[u_1(t) - u_2(t)] + 2r_1 D_1 (i_2(t) + i_3(t)) + 2r_2 D_2 i_2(t)}{2r_1 \sum i(t) + \frac{l_1 \sum v_L(t)}{L}} \\ &\quad + \frac{\frac{l_2 D_2 v_{L2}(t)}{L} + \frac{l_1 D_1 (v_{L2}(t) + v_{L3}(t))}{L}}{2r_1 \sum i(t) + \frac{l_1 \sum v_L(t)}{L}} \end{aligned} \qquad (6)$$

Here $\sum v_L(t) = v_{L1}(t) + v_{L2}(t) + v_{L3}(t)$. Similarly, rearranging (3) and (5) define the fault distance from bus 1 considering bus 3 of node 1, given as (7).

$$\begin{aligned} &x|_{B_3,N_1} = \frac{[u_1(t) - u_3(t)] + 2r_1 D_1 (i_2(t) + i_3(t))}{2r_1 \sum i(t) + \frac{l_1 \sum v_L(t)}{L}} \\ &\quad + \frac{2 (r_3 D_3 + M_1 r_{M1}) i_3(t)}{2r_1 \sum i(t) + \frac{l_1 \sum v_L(t)}{L}} \\ &\quad + \frac{\frac{(l_3 D_3 + M_1 l_{M1}) v_{L3}(t)}{L} + \frac{l_1 D_1 (v_{L2}(t) + v_{L3}(t))}{L}}{2r_1 \sum i(t) + \frac{l_1 \sum v_L(t)}{L}} \end{aligned} \qquad (7)$$

The equivalent calculated fault location is defined as $x|_{SL_1}$, given by $x|_{SL_1} = \frac{x|_{B_2,N_1} + x|_{B_3,N_1}}{2}$. This is done to reduce random uncertainty in measurement [25] and increase fault location reliability. Here $x|_{B_2,N_1} - x|_{B_3,N_1} \approx 0$ and $\boldsymbol{x} \leq D_1$: $\boldsymbol{x} \in \{x|_{B_2,N_1}, x|_{B_3,N_1}\}$ are two verification conditions for better reliability. These are validated using Fig. 4, showing a fault at 0.5 km at SL_1. Either of the two terminals, along with the
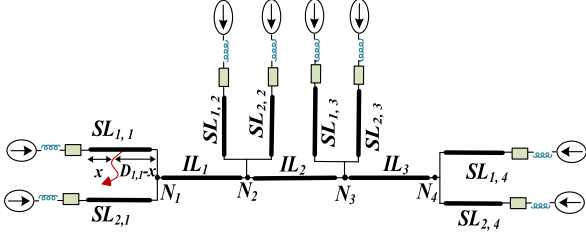
Fig. 5. *4 node, 8 bus* MVDC system.

faulty terminal, can be used to calculate accurate fault location. The algorithm's reliability increases if the number of terminals is used to calculate fault location. $X|_{B_n,N_m}$ in Fig. 4 shows the calculated location for a short-circuit fault ($R_f = 0\,\Omega$) using bus n and node m whereas $x|_{B_n,N_m}$ shows the variation of $X|_{B_n,N_m}$ with a rolling mean filter having a moving window of 20 sample steps [16]. Throughout the analysis, $x|_{B_n,N_m}$ is used to represent the filtered value of calculated location, $X|_{B_n,N_m}$. Similar analysis can be carried out for faults at SL_2 and SL_3 respectively.

2) Fault at IL_1: If the fault is located at IL_1, given as F_3 in Fig. 2, (8) and (9) are obtained considering bus 3 and bus 1.

$$2r_3D_3i_3(t) + 2l_3D_3\frac{di_3}{dt} + 2dr_{M1}i_3(t) + 2l_{M1}v_{L3}\frac{di_3}{dt}$$
$$+ R_f\sum i(t) = u_3(t) \qquad (8)$$

$$2r_1D_1i_1(t) + l_1D_1\frac{di_1}{dt} + 2(M_1 - x)r_{M1}(i_1(t) + i_2(t))$$
$$+ (M_1 - x)l_{M1}\left[\frac{di_1}{dt} + \frac{di_2}{dt}\right] + R_f\sum i(t) = u_1(t) \quad (9)$$

Fault distance from bus 3 considering bus 1 is given as (10) shown at the bottom of this page.

Similar analysis can be carried out using KVL considering bus 2 and bus 3 to obtain $x|_{B_2,N_1}$. This gives the equivalent calculated fault location, $x|_{IL_1} = \frac{x|_{B_1,N_1} + x|_{B_2,N_1}}{2}$. Here $x|_{B_1,N_1} - x|_{B_2,N_1} \approx 0$ and $x \leq M_1$: $x \in \{x|_{B_1,N_1}, x|_{B_2,N_1}\}$.

B. Fault Location for a 4 Node, 8 Bus System

If the fault is located at $SL_{1,1}$, the single-line 4 node, 8 bus system is given as shown in Fig. 5. The unit resistance and inductance related to $SL_{j,i}$ is given as $r_{j,i}$ and $l_{j,i}$. $D_{j,i}$ is the total length of source/load line, $SL_{j,i}$. Using KVL for a PTP fault at $SL_{1,1}$, (11)–(15) are obtained considering bus 1 of node 1, bus 2 of node 1, bus 1 of node 2 and bus 1 of node 3.

$$2r_{1,1}xi_{1,1}(t) + 2l_{1,1}x\frac{di_{1,1}(t)}{dt} + R_f\sum i(t) = u_{1,1}(t) \quad (11)$$

$$2D_{2,1}r_{2,1}i_{2,1}(t) + 2l_{2,1}D_{2,1}\frac{di_{2,1}(t)}{dt}$$
$$+ 2(D_{1,1} - x)r_{1,1}\left[\sum i(t) - i_{1,1}(t)\right]$$
$$+ 2l_{1,1}(D_{1,1} - x)\left(\frac{d\sum i(t)}{dt} - \frac{di_{1,1}(t)}{dt}\right)$$
$$+ R_f\sum i(t) = u_{2,1}(t) \qquad (12)$$

$$2D_{1,2}r_{1,2}i_{1,2}(t) + 2M_1r_{M1}\left[\sum i(t) - i_{1,1}(t) - i_{2,1}(t)\right]$$
$$+ 2l_{1,2}D_{1,2}\frac{di_{1,2}(t)}{dt}$$
$$+ 2M_1l_{M1}\left(\frac{d\left[\sum i(t) - i_{1,1}(t) - i_{2,1}(t)\right]}{dt}\right)$$
$$+ 2(D_{1,1} - x)r_{1,1}\left[\sum i(t) - i_{1,1}(t)\right]$$
$$+ 2l_{1,1}(D_{1,1} - x)\left(\frac{d\left[\sum i(t) - i_{1,1}(t)\right]}{dt}\right)$$
$$+ R_f\sum i(t) = u_{1,2}(t) \qquad (13)$$

$$2D_{1,3}r_{1,3}i_{1,3}(t) + 2M_1r_{M1}\left[\sum i(t) - i_{1,1}(t) - i_{2,1}(t)\right]$$
$$+ 2M_2r_{M2}\left[i_{1,3}(t)\right.$$
$$\left.+ i_{2,1}(t)\right] + 2l_{1,3}D_{1,3}\frac{di_{1,3}(t)}{dt}$$
$$+ 2M_1l_{M1}\left(\frac{d\left[\sum i(t) - i_{1,1}(t) - i_{2,1}(t)\right]}{dt}\right)$$
$$+ 2M_2l_{M2}\left(\frac{d\left[i_{1,3}(t) + i_{2,3}(t)\right]}{dt}\right)$$
$$+ 2(D_{1,1} - x)r_{1,1}\left[\sum i(t) - i_{1,1}(t)\right]$$
$$+ 2l_{1,1}(D_{1,1} - x)\left(\frac{d\left[\sum i(t) - i_{1,1}(t)\right]}{dt}\right)$$
$$+ R_f\sum i(t) = u_{1,3}(t) \qquad (14)$$

Rearranging (11) and (12) define the fault distance from bus 1 of node 1 considering bus 2 of node 1, given as (15) shown at the bottom of the next page.

Similarly, rearranging (11) and (13) defines the fault distance from bus 1 of node 1 considering bus 1 of node 2, given as (16) shown at the bottom of the next page.

On similar lines, rearranging (11) and (14) define the fault distance from bus 1 of node 1 considering bus 1 of node 3, given as (17) shown at the bottom of the next page. Further, similar

$$x|_{B_1,N_1} = \frac{[u_3(t) - u_1(t)] + 2r_1D_1i_1(t) + 2[r_3D_3 + M_1r_{M1}](i_1(t) + i_2(t))}{2r_{M1}\sum i(t) + \frac{l_{M1}\sum v_L(t)}{L}}$$
$$+ \frac{\frac{l_1D_1v_{L1}}{L} + \frac{[M_1l_{M1} + D_3l_3](v_{L1}(t) + v_{L2}(t))}{L}}{2r_{M1}\sum i(t) + \frac{l_{M1}\sum v_L(t)}{L}} - \frac{2r_3D_3\sum i(t) + \frac{l_3D_3\sum v_L(t)}{L}}{2r_{M1}\sum i(t) + \frac{l_{M1}\sum v_L(t)}{L}} \qquad (10)$$

analysis can be performed for faults at different $SL_{j,i}$ and IL_{i-1} respectively.

C. Fault Location for a Generalized k Node, p Bus System

Fig. 6(a) shows a generalized p bus, k node radial MVDC system. Fault at source/load line is shown to occur at node i (N_i), bus j (given as $SL_{j,i}$, shown as F_1 in Fig. 6(b)). Fault at interconnecting line occurs between node $i\text{-}1$ and i is shown as F_2 in Fig. 6(c). The algorithm can be applied based on a system's availability of communication and sensors with multiple terminal measurements available, and the location reliability increases, as highlighted earlier.

Furthermore, given the inductive nature of the fault location estimation described in Sections IV-A and IV-B, we can formulate the following theorem for the general location of the $SL_{j,i}$.

Theorem 1: For the generalized MVDC power system depicted in Fig. 6, fault at the $SL_{j,i}$, for $j \in \{1, \ldots, N_p\}$ and $i \in \{1, \ldots, k\}$ can always be described with the (18a) shown at the bottom of the next page.

The proof for this theorem is in Appendix A. The results of Theorem 1 can be further elaborated to cover fault location at IL_{i-1}.

Theorem 2: For the generalized MVDC power system depicted in Fig. 6, the fault placed at any interconnecting line between nodes $i-1$ and i, for $i \in \{1, \ldots, k\}$, can be determined using formula (18b).

The proof for this theorem is given in Appendix B.

V. PROPOSED FAULT LOCATION SCHEME

To start with, the terminal voltage data, along with the voltage and current data across different CLRs, are measured. Further,

a rolling mean filter (window of 50 samples) is used to filter out the high-frequency WGN in the measurement. Further, the DCR is used to identify if there is a fault in the system. If there is a violation of I_{set}, specific faulty segment is identified (between $SL_{j,i}$ and IL_i). For a fault at $SL_{j,i}$, (18a) is used for calculating the fault distance, whereas for a fault at IL_i, (18b) is used to calculate the fault distance. Fault location is calculated considering each bus and node (excluding the case where $(p,k) = (j,i)$ i.e., the location from bus j considering bus j, node i). This means that the method entirely focuses on multi-terminal measurements for fault location. Once the fault location is calculated, conditions (22) are verified. If (22) is satisfied, the final fault location is evaluated using (21). Fig. 7 shows the layout of the proposed fault location scheme.

VI. RESULTS AND VALIDATION

The test systems shown in Figs. 1 and 2 are implemented using PSCAD/EMTDC based electromagnetic transient simulations. A sampling frequency, f_s of 50 kHz is used for conclusive plots. However, Section V(D) shows that a sampling frequency of 5 kHz is enough for satisfactory accuracy. The detailed models of OHL and UGC are considered in PSCAD/EMTDC. The parameters for the test system are given in Table II. The validation starts with fault identification and eventually the location of the fault in a three-bus system shown in Fig. 2. Once the process of fault location is validated for a smaller system, it is then tested for a six-bus system shown in Fig. 1. The algorithm is further tested under different fault resistances and fault locations with different sampling frequencies and white Gaussian noise (WGN) in measurement. Finally, the effect of parameter variation on the proposed algorithm is discussed.

$$x|_{B_2,N_1} = \frac{[u_{1,1}(t) - u_{2,1}(t)] + 2r_{1,1}D_{1,1}\left(\sum i(t) - i_{1,1}(t)\right) + 2r_{2,1}D_{2,1}i_{2,1}(t)}{2r_{1,1}\sum i(t) + \frac{l_{1,1}\sum v_L(t)}{L}}$$

$$+ \frac{\frac{l_{2,1}D_{2,1}v_{L2,1}(t)}{L} + \frac{l_{1,1}D_{1,1}(\sum v_L(t) - v_{L1,1}(t))}{L}}{2r_{1,1}\sum i(t) + \frac{l_{1,1}\sum v_L(t)}{L}} \tag{15}$$

$$x|_{B_1,N_2} = \frac{[u_{1,1}(t) - u_{1,2}(t)] + 2r_{1,1}D_{1,1}\left(\sum i(t) - i_{1,1}(t)\right) + 2r_{1,2}D_{1,2}i_{1,2}(t)}{2r_{1,1}\sum i(t) + \frac{l_{1,1}\sum v_L(t)}{L}}$$

$$+ \frac{\frac{l_{1,2}D_{1,2}v_{L1,2}(t)}{L} + \frac{l_{1,1}D_{1,1}(\sum v_L(t) - v_{L1,1}(t))}{L}}{2r_{1,1}\sum i(t) + \frac{l_{1,1}\sum v_L(t)}{L}} \tag{16}$$

$$x|_{B_1,N_3} = \frac{[u_{1,1}(t) - u_{1,3}(t)]}{2r_{1,1}\sum i(t) + \frac{l_{1,1}\sum v_L(t)}{L}}$$

$$+ \frac{\frac{l_{1,3}D_{1,3}v_{L1,3}(t)}{L} + \frac{l_{1,1}D_{1,1}(\sum v_L(t) - v_{L1,1}(t))}{L} + \frac{M_1 l_{M1}(\sum v_L(t) - v_{L1,1}(t) - v_{L2,1}(t))}{L} + \frac{M_2 l_{M2}(v_{L1,3}(t) - v_{L2,3}(t))}{L}}{2r_{1,1}\sum i(t) + \frac{l_{1,1}\sum v_L(t)}{L}}$$

$$+ \frac{2r_{1,1}D_{1,1}\left(\sum i(t) - i_{1,1}(t)\right) + 2r_{1,3}D_{1,3}i_{1,3}(t) + 2M_1 r_{M1}\left(\sum i(t) - i_{1,1}(t) - i_{2,1}(t)\right) + 2M_2 r_{M2}[i_{1,3}(t) + i_{2,3}(t)]}{2r_{1,1}\sum i(t) + \frac{l_{1,1}\sum v_L(t)}{L}} \tag{17}$$
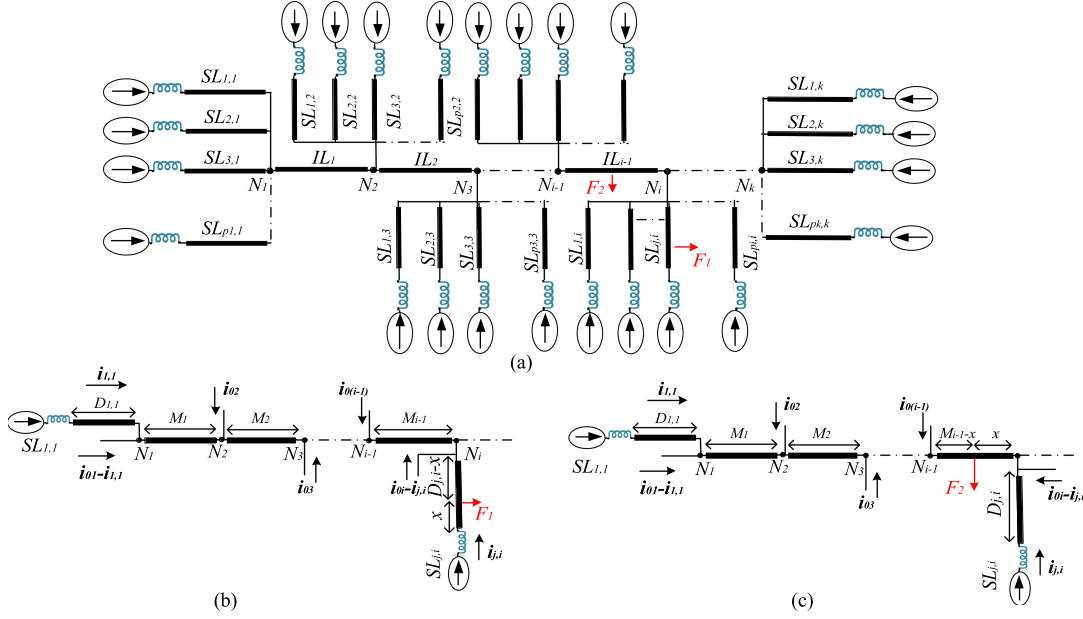
Fig. 6.   (a) Generalised *k node, p bus* MVDC system, (b) effective circuit for fault, F₁, and (c) effective circuit for fault, F₂.

TABLE II
PARAMETERS FOR A TEST SYSTEM IN PSCAD/EMTDC

DC Voltage *(kV)*	± 2
DC link capacitance (2C) *(mF)*	15.6
Grounding resistance (R_g) (Ω)	0.2-0.5
Smoothing Reactor *(mH)*	1
Parameters of OHL	Resistance [Ω/km]: 0.132
	Inductance [mH/km]: 0.201
	Capacitance [μF/km]: 0.011
Parameters of UGC	Resistance [Ω/km]: 0.098
	Inductance [mH/km]: 0.074
	Capacitance [μF/km]: 0.272

A. Validation for Fault Location for a Three Bus System

A three-bus system with SL_1-SL_3 and IL_1 is used (see Fig. 2) to check the performance of the fault identification and location

algorithm. Different types of faults (PTP, P-PTG and N-PTG) occur at the source/load line and interconnecting line.

1) Source/Load Line Faults:

a) PTP fault: A PTP fault occurs at $d = 0.5$ km at SL_1 with fault resistance, $R_f = 1\,\Omega$. Both positive and negative pole differential current ($i_{B1,1^+}(t)$ and $i_{B1,1^-}(t)$) violate I_{set} indicating a PTP fault at SL_1. The differential current of other terminals does not violate I_{set}. Once the fault is identified in lesser than 1 ms, the fault location algorithm calculates $X|_{B_2,N_1}$ and $X|_{B_3,N_1}$, $x|_{B_2,N_1}$ and $x|_{B_3,N_1}$ (rolling mean of $X|_{B_2,N_1}$ and $X|_{B_3,N_1}$). Over 1–2 ms of fault inception, Fig. 8(a) shows $x|_{B_3,N_1} \approx 0.496$ km, $x|_{B_2,N_1} \approx 0.508$ km and $x|_{B_2,N_1}$-$x|_{B_3,N_1} \approx 0.012$ km.

b) P-PTG faults: A P-PTG fault occurs at $d = 0.25$ km at SL_1 with fault resistance, $R_f = 1\,\Omega$ and grounding resistance, $R_g = 0.5\,\Omega$. Only positive pole differential current

$$x|_{B_n,N_m} = \frac{[u_{j,i}(t) - u_{n,m}(t)] + 2r_{n,m}D_{n,m}i_{n,m}(t) + 2\sum_{\beta=m}^{i-1} M_\beta r_{M_\beta} \sum_{\varepsilon=m}^{\beta} i_{0\varepsilon} + 2D_{j,i}r_{j,i} \atop \sum_{(\alpha,\beta)=(1,1) \atop (\alpha,\beta)\neq(j,i)}^{p_{\beta},k} i_{\alpha,\beta}(t) + l_{n,m}D_{n,m}\frac{v_{L_{n,m}}(t)}{L_{n,m}} + \sum_{\beta=m}^{i-1} l_{M_\beta} M_\beta \sum_{(\alpha,\varepsilon)=(1,m)}^{p_{i-1},\beta} \frac{v_{L_{\alpha,\varepsilon}}(t)}{L_{\alpha,\varepsilon}} + D_{j,i}l_{j,i} \sum_{(\alpha,\beta)=(1,1) \atop (\alpha,\beta)\neq(j,i)}^{p_{\beta},k} \frac{v_{L_{\alpha,\beta}}(t)}{L_{\alpha,\beta}}}{2r_{j,i}\sum i(t) + l_{j,i}\sum \frac{v_{L_{j,i}}}{L_{j,i}}}$$

$$(18a)$$

$$x|_{B_n,N_m} = \frac{[u_{j,i}(t) - u_{n,m}(t)] + 2r_{n,m}D_{n,m}i_{n,m}(t) + 2\sum_{\beta=m}^{i-2} M_\beta r_{M_\beta} \sum_{\varepsilon=m}^{\beta} i_{0\varepsilon} + 2M_{i-1}r_{M_{i-1}} \sum_{\varepsilon=m}^{i-1} i_{0\varepsilon}(t) \atop + l_{n,m}D_{n,m}\frac{v_{L_{n,m}}(t)}{L_{n,m}} + \sum_{\beta=m}^{i-2} l_{M_\beta} M_\beta \sum_{(\alpha,\varepsilon)=(1,m)}^{p_{i-2},\beta} \frac{v_{L_{\alpha,\varepsilon}}(t)}{L_{\alpha,\varepsilon}} + M_{i-1}l_{M_{i-1}} \sum_{(\alpha,\beta)=(1,1)}^{p_{\beta},i-1} \frac{v_{L_{\alpha,\beta}}(t)}{L_{\alpha,\beta}}}{2r_{M_{i-1}}\sum i(t) + l_{M_{i-1}}\sum \frac{v_{L_{j,i}}}{L_{j,i}}}$$

$$-\frac{2r_{j,i}D_{j,i}i_{j,i}(t) + l_{j,i}D_{j,i}\frac{v_{L_{j,i}}(t)}{L_{j,i}}}{2r_{M_{i-1}}\sum i(t) + l_{M_{i-1}}\sum \frac{v_{L_{j,i}}}{L_{j,i}}}$$
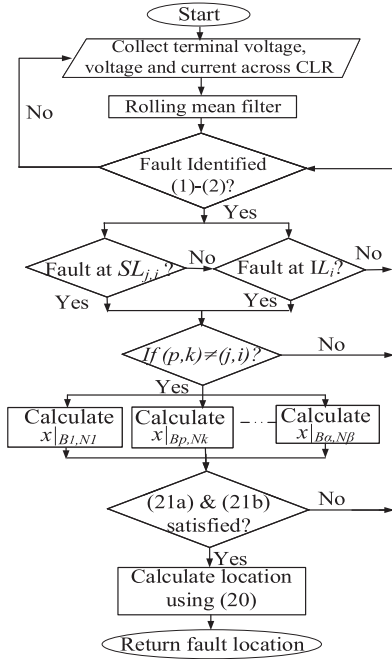
$$(18b)$$

Fig. 7.   Layout of the scheme.

$(i_{B1,1+}(t))$ violates I_{set} indicating a P-PTG fault at SL_1. Fig. 8(b) shows $x|_{B_3,N_1} \approx 0.251$ km, $x|_{B_2,N_1} \approx 0.254$ km and $x|_{B_2,N_1}$-$x|_{B_3,N_1} \approx 0.003$ km.

c) N-PTG fault: A N-PTG fault occurs at $d = 0.75$ km at SL_1 with fault resistance, $R_f = 1\,\Omega$ and grounding resistance, $R_g = 0.5\,\Omega$. The differential negative pole current $(i_{B1,1-}(t))$ violates I_{set} indicating a N-PTG. Once the fault is identified, the location is calculated as $x|_{B_3,N_1} \approx 0.755$ km, $x|_{B_2,N_1} \approx 0.763$ km and $x|_{B_2,N_1}$-$x|_{B_3,N_1} \approx 0.008$ km.

2) Interconnecting Line Faults:

a) PTP fault: A PTP fault occurs at $d = 5$ km at IL_1. Both positive and negative pole differential current $(i_{B1,1+}(t)$ and $i_{B1,1-}(t))$ violate I_{set} indicating a PTP fault at IL_1. Fig. 9(a) shows $x|_{B_3,N_1} \approx 4.995$ km, $x|_{B_2,N_1} \approx 4.99$ km and $x|_{B_2,N_1}$-$x|_{B_3,N_1} \approx -0.005$ km.

b) P-PTG faults: A P-PTG fault occurs at $d = 3$ km at IL_1, with grounding resistance, $R_g = 0.5\,\Omega$. Only positive pole differential current $(i_{B1,1+}(t))$ violates I_{set} indicating a P-PTG fault at IL_1. Fig. 9(b) shows $x|_{B_3,N_1} \approx 3.005$ km, $x|_{B_2,N_1} \approx 2.995$ km and $x|_{B_2,N_1}$-$x|_{B_3,N_1} \approx -0.01$ km.

c) N-PTG fault: A N-PTG fault occurs at $d = 6$ km at IL_1 with fault resistance, $R_f = 5\,\Omega$ and grounding resistance, $R_g = 0.5\,\Omega$. Only the differential negative pole current $(i_{B1,1-}(t))$ violates I_{set} indicating a N-PTG at IL_1. The location is calculated as $x|_{B_3,N_1} \approx 6.002$ km, $x|_{B_2,N_1} \approx 5.99$ km and $x|_{B_2,N_1}$-$x|_{B_3,N_1} \approx -0.012$ km.

B. Validation for Fault Location in a Six Bus System

For the system shown in Fig. 1, the inception of different faults at $SL_{1,1}$ and IL_1 occur to validate the fault location algorithm for a six-bus test system.

1) Source/Load Line Faults: Fig. 8 shows different faults at $SL_{1,1}$ (total length 2 km). Fig. 10(a) shows the calculated fault location for a fault at $d = 0.05$ km. The fault location calculated from bus 1 considering different buses and nodes are $x|_{B_2,N_1} \approx 0.051$ km, $x|_{B_3,N_1} \approx 0.053$ km, $x|_{B_4,N_1} \approx 0.055$ km, $x|_{B_5,N_1} \approx 0.053$ km, and $x|_{B_6,N_1} \approx 0.052$ km. Using (21), $x|_{SL_{1,1}} = 0.0528$ km. Fig. 10(b) shows the calculated fault location for a fault at $d = 1$ km. The location with different buses and nodes are $x|_{B_2,N_1} \approx 1.001$ km, $x|_{B_3,N_1} \approx 1.002$ km, $x|_{B_4,N_1} \approx 1.0025$ km, $x|_{B_5,N_1} \approx 1.002$ km, $x|_{B_6,N_1} \approx 1.002$ km. Using (21), $x|_{SL_{1,1}} = 1.0019$ km. Fig. 10(c) shows the calculated fault location for a fault at $d = 1.95$ km. The location calculated with different buses and nodes are $x|_{B_2,N_1} \approx 1.946$ km, $x|_{B_3,N_1} \approx 1.9475$ km, $x|_{B_4,N_1} \approx 1.95$ km, $x|_{B_5,N_1} \approx 1.9475$ km, and $x|_{B_6,N_1} \approx 1.947$ km. Using (21), $x|_{SL_{1,1}} = 1.9476$ km.

2) Interconnecting Line Faults: Fig. 11 shows different faults at IL_1 (total length 10 km). Fig. 11(a) shows the calculated fault location for a fault at $d = 2$ km. Similar to (15), $x|_{IL_1} = 2.006$ km. Fig. 11(b) shows location for a fault at $d = 4$ km as $x|_{IL_1} = 4.008$ km and Fig. 11(c) shows location for a fault at $d = 6$ km as $x|_{IL_1} = 6.003$ km. Similar to faults at $SL_{1,1}$, the calculated location is accurate.

C. Validation for Different Fault Resistances

The variation of calculated location with different fault resistances (up to $R_f = 200\,\Omega$) is explored in Table III. Since the method is multi-terminal, the algorithm's accuracy is independent of fault resistance. Table III shows faults at $SL_{1,2}$, and IL_2. Considering Fig. 1 as a test system, there are 5 buses which can be individually used to calculate the fault location for $SL_{1,2}$ (i.e., $x|_{B_4,N_2}, x|_{B_5,N_2}, x|_{B_6,N_2}, x|_{B_1,N_2}$ and $x|_{B_2,N_2}$). Similarly, for a fault at IL_1, $x|_{B_1,N_2}, x|_{B_2,N_2}, x|_{B_3,N_2}, x|_{B_4,N_2}, x|_{B_5,N_2}$, and $x|_{B_5,N_2}$ can be used. However, due to space constraints, Table III shows the fault location using 3 buses for each case. For high sampling frequencies ($f_s > 20$ kHz), there is no loss of accuracy for high fault resistances. For low sampling frequencies ($f_s < 20$ kHz), there is a marginal loss of accuracy ($< 1\%$) for high fault resistances. This is because as fault resistance increases, the signal damping increases. If the sampling frequency is less, useful samples are passed over.

D. Performance Under Different Sampling Frequencies

Fault location accuracy with low sampling frequency can help in cost-effective hardware implementation. Table IV shows that a 5 kHz sampling frequency gives satisfactory results for the proposed fault location method. However, as evident from Table IV, higher f_s means more useful samples, which increase the accuracy of the fault location algorithm.

E. Fault Location Calculation With Parameter Variation

The sensitivity of the fault location algorithm with the variation of system parameters, i.e., r (unit resistance) and l (unit inductance) of cables and C (DC link capacitance) of converters is explored. The initial parameters are given in Table II. It is observed that using different values of r and C up to $\pm 200\%$
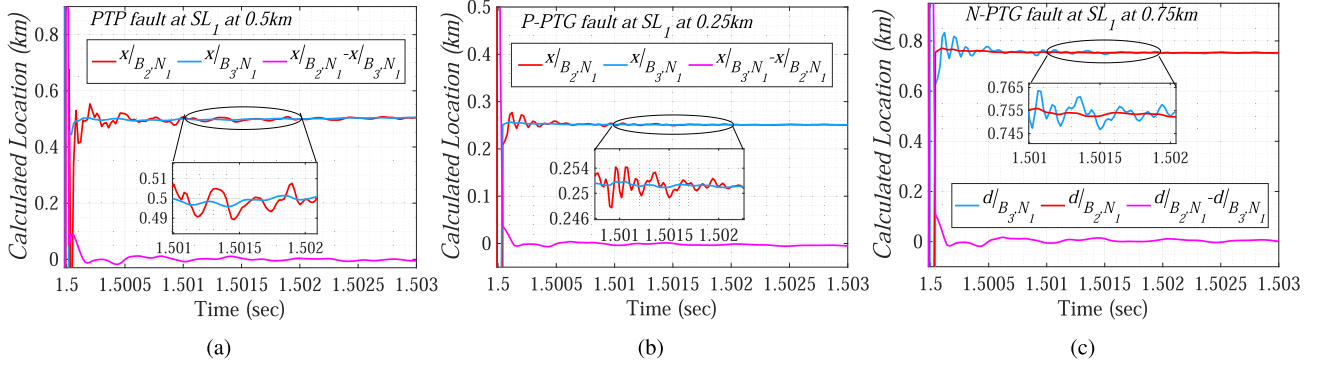
Fig. 8. Three-bus system: Calculated fault location for different faults at SL_1 at (a) $d = 0.5$ km; (b) $d = 0.25$ km; (c) $d = 0.75$ km.
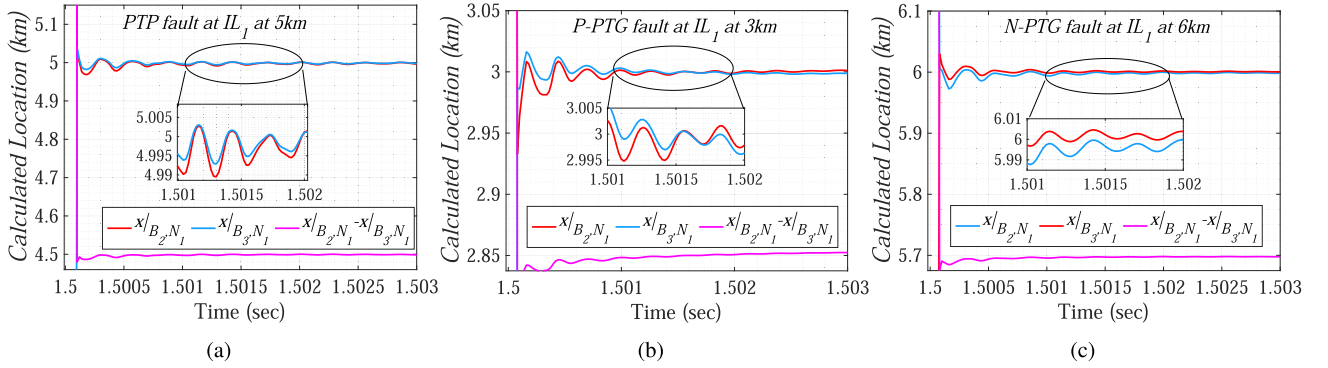

Fig. 9. Three-bus system: Differential current and calculated fault location for different faults at IL_1 at (a) $d = 5$ km; (b) $d = 3$ km; (c) $d = 6$ km.
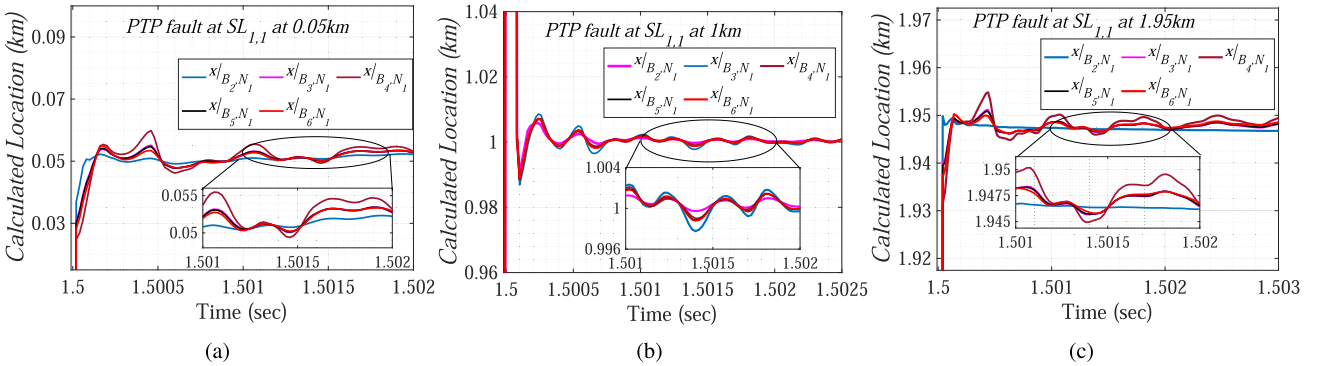

Fig. 10. Six-bus system: Calculated fault location for faults at $SL_{1,1}$ at (a) $d = 0.05$ km, (b) $d = 1$ km, (c) $d = 1.95$ km.

does not change the accuracy of the fault location algorithm. However, the accuracy of the algorithm varies with variations in unit inductance. Table V shows $\varepsilon(\%) = \varepsilon/x$ with % change in inductance value. For faults closer to the bus terminal, % drop in fault location accuracy is higher. As a result, a $\pm 20\%$ change in inductance reduces accuracy as high as $\pm 18\%$. This suggests that the fault location method is sensitive to the unit inductance of the line or cable. In contrast, unit resistance and DC link capacitance value do not affect it.

The future scope of work includes analyzing the variation of fault location accuracy concerning change in unit inductance

in detail and proposing a location method with much lesser sensitivity due to its interpretation.

F. Fault Detection and Location Time

For the application of the proposed location method, the fault identification scheme takes around 1 ms, which complements the location method. For $f_s = 20$ kHz, maximum identification time is recorded as 0.95 ms. The fault location window is 1 to 2 ms from the inception time. This makes the method's maximum detection and location time to be less than 2 ms.
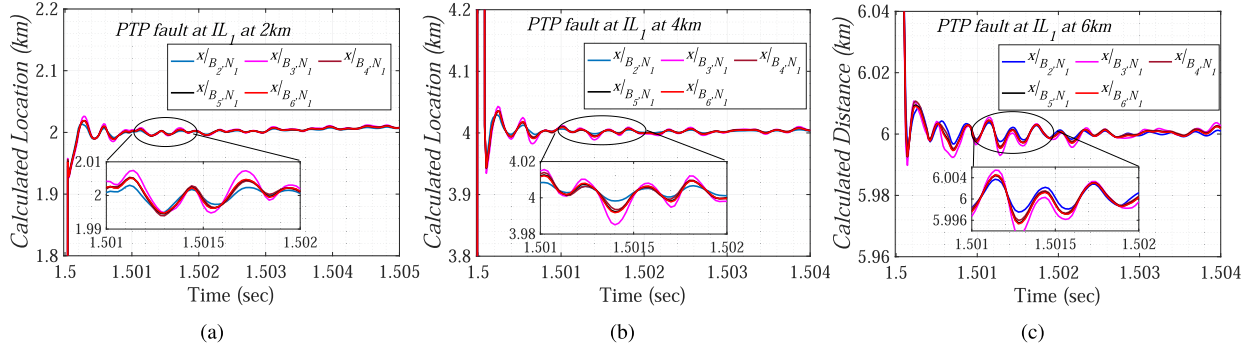
Fig. 11. Six-bus system: Calculated fault location for faults at IL_1 at (a) $d = 2$ km, (b) $d = 4$ km, (c) $d = 6$ km.

TABLE III
VARIATION OF CALCULATED FAULT LOCATION (KM) WITH FAULT RESISTANCE, R_f (Ω) FOR DIFFERENT FAULTS (PTG, PTP) AT DIFFERENT LOCATIONS

	$SL_{1,2}$ (Total Length: 1km)									IL_1 (Total Length: 10km)								
	R_f=0.01Ω			R_f=50Ω			R_f=200Ω			R_f=0.01Ω			R_f=50Ω			R_f=200Ω		
	$x\|_{B_4,N_2}$	$x\|_{B_5,N_2}$	$x\|_{B_6,N_2}$	$x\|_{B_4,N_2}$	$x\|_{B_5,N_2}$	$x\|_{B_6,N_2}$	$x\|_{B_4,N_2}$	$x\|_{B_5,N_2}$	$x\|_{B_6,N_2}$	$x\|_{B_4,N_2}$	$x\|_{B_5,N_2}$	$x\|_{B_6,N_2}$	$x\|_{B_4,N_2}$	$x\|_{B_5,N_2}$	$x\|_{B_6,N_2}$	$x\|_{B_4,N_2}$	$x\|_{B_5,N_2}$	$x\|_{B_6,N_2}$
P-PTG																		
5%	0.052	0.053	0.05	0.052	0.052	0.052	0.054	0.055	0.052	0.505	0.502	0.502	0.510	0.505	0.505	0.515	0.51	0.512
30%	0.312	0.318	0.297	0.295	0.318	0.315	0.29	0.322	0.32	3.05	3.08	3.02	3.05	3.1	2.97	3.12	3.05	2.92
45%	0.45	0.452	0.462	0.455	0.448	0.462	0.455	0.446	0.46	4.505	4.51	4.492	4.51	4.51	4.495	4.51	4.51	4.485
60%	0.6	0.622	0.615	0.605	0.62	0.62	0.61	0.625	0.625	6.1	6.1	5.85	6.15	6.22	6.15	6.15	6.1	6.25
75%	0.755	0.76	0.748	0.762	0.762	0.755	0.765	0.77	0.762	7.51	7.5	7.525	7.51	7.51	7.52	7.52	7.51	7.62
95%	0.95	0.955	0.945	0.958	0.96	0.965	0.938	0.955	0.97	9.5	9.52	9.51	9.54	9.58	9.62	9.45	9.4	9.655
N-PTG																		
5%	0.052	0.053	0.05	0.052	0.052	0.052	0.054	0.055	0.052	0.505	0.502	0.502	0.510	0.505	0.505	0.515	0.51	0.512
30%	0.312	0.318	0.297	0.295	0.318	0.315	0.29	0.322	0.32	3.05	3.08	3.02	3.05	3.1	2.97	3.12	3.05	2.92
45%	0.45	0.452	0.462	0.455	0.448	0.462	0.455	0.446	0.46	4.505	4.51	4.492	4.51	4.51	4.495	4.51	4.51	4.485
60%	0.6	0.622	0.615	0.605	0.62	0.62	0.61	0.625	0.625	6.1	6.1	5.85	6.15	6.22	6.15	6.15	6.1	6.25
75%	0.755	0.76	0.748	0.762	0.762	0.755	0.765	0.77	0.762	7.51	7.5	7.525	7.51	7.51	7.52	7.52	7.51	7.62
95%	0.95	0.955	0.945	0.958	0.96	0.965	0.938	0.955	0.97	9.5	9.52	9.51	9.54	9.58	9.62	9.45	9.4	9.655
PTP																		
5%	0.051	0.0525	0.05	0.052	0.0535	0.052	0.054	0.0545	0.052	0.505	0.502	0.502	0.510	0.51	0.505	0.515	0.51	0.512
30%	0.32	0.32	0.297	0.29	0.318	0.315	0.33	0.322	0.32	3.06	3.12	3.12	3.05	3.1	2.97	3.12	3.05	2.92
45%	0.455	0.45	0.462	0.455	0.448	0.462	0.455	0.446	0.46	4.505	4.51	4.492	4.51	4.51	4.495	4.51	4.51	4.485
60%	0.62	0.622	0.615	0.605	0.62	0.62	0.61	0.625	0.625	6.05	5.95	5.85	6.15	6.22	6.15	6.15	6.1	6.25
75%	0.762	0.76	0.748	0.762	0.762	0.755	0.765	0.77	0.762	7.51	7.5	7.525	7.51	7.51	7.52	7.52	7.51	7.62
95%	0.962	0.955	0.945	0.958	0.96	0.965	0.938	0.955	0.97	9.55	9.52	9.51	9.54	9.58	9.62	9.45	9.4	9.655

TABLE IV
LOCATION WITH DIFFERENT SAMPLING FREQUENCIES FOR A PTP FAULT AT $SL_{1,2}$

Error (m)=Fault Location-Calculated Fault Location				
Fault Location (m)	50kHz	20kHz	10kHz	5kHz
100	1.25	3.35	6.56	10.05
300	1.18	3.32	6.63	11.54
500	0.75	3.22	6.58	10.45
700	1.15	3.27	5.77	9.82
900	1.12	3.32	5.92	9.68

TABLE VI
FAULT LOCATION IN THE PRESENCE OF WGN

	Error (m)			
Fault Location (m)	10dB	20dB	30dB	40dB
100	7.25	4.42	4.76	2.55
300	6.18	4.35	3.85	2.62
500	6.75	5.02	4.52	2.55
700	7.15	4.34	3.82	2.71
900	7.12	5.3	2.92	2.35

TABLE V
VARIATION OF CALCULATED FAULT LOCATION ERROR (%) WITH VARIATION IN UNIT INDUCTANCE (%) FOR A PTP FAULT AT $SL_{1,1}$

Calculated Fault Location error (%)=ε/x					
	Fault Distance, x (m)				
Variation in l	100m	500m	900m	1300m	1700m	1900m
±5%	4.2%	1.24%	0.67%	0.45%	0.35%	0.31%
±10%	10.1%	2.35%	1.36%	0.88%	0.71%	0.62%
±15%	15.4%	3.94%	2.05%	1.32%	1.02%	0.97%
±20%	18.1%	4.84%	2.65%	1.81%	1.34%	1.28%

G. Performance With White Gaussian Noise in Measurement

White Gaussian Noise (WGN) in the measurement induces high-frequency components in the measured current and voltage data. This can cause inaccuracy in the results for the fault location of the proposed scheme. As a result, a rolling mean filter [16] is used with a moving window of 50 sample steps for voltage and current samples. Additionally, another rolling mean is used with a window of 20 samples to smoothen the fault location curve (see Fig. 4). WGN is random with the property of zero mean [16]. Using rolling mean samples effectively eliminates the effect of WGN to a great extent without affecting the accuracy of the proposed fault location algorithm. Table VI performs the algorithm with WGN in measurement for a PTP fault at SL_1. A first-order lag can also be used in place of a rolling mean if the delay due to the lag filter does not hinder the stringent requirement of fault detection and location time.

VII. CONCLUSION

The work proposes a novel fault location algorithm for a multi-terminal radial MVDC microgrid. Based on the findings of the proposed work, it is concluded that:

- The proposed algorithm locates the fault distance in a system ranging from a simple homogeneous line configuration to n-segment non-homogeneous lines for distribution i.e., different line/cable combinations.
- Any of the bus terminals along with the faulty bus terminal can be used to accurately locate the fault. If other bus terminals are also utilized (subject to the availability of communication and sensors) for fault location, the reliability of the method increases.
- The proposed analysis of fault location is extrapolated and generalized for a comparatively larger MVDC system with k node and p bus for wider applications to different systems.
- The proposed method is sensitive to the use of the true value of the unit inductance of a line or cable. A 20% deviation in the true value of unit inductance can cause location error as high as 18%. The error is relatively higher for faults closer to the bus terminal. The accuracy of the method is not affected by even $\pm 200\%$ change in the unit resistance of the line or cable and the value of DC link capacitance.
- The performance of the location method is robust for different sampling frequencies ($f_s = 5$–100 kHz), under different WGN in measurement (SNR = 0–40 dB), for different types of faults (PTP, P-PTG, and N-PTG) at different fault resistances (validated up to $R_f = 200\,\Omega$) and location.

APPENDIX A
GENERALITY FOR FAULT LOCATION AT $\text{SL}_{j,i}$

Proof: Each node, n in the generalized system is considered to have p_n buses contributing a total fault current of $i_{0n}(t)$. Here fault current from bus 1 at node n is indicated as $i_{1,n}(t)$. Similarly, current from bus 2 at node n is indicated as $i_{2,n}(t)$ and so on. The total fault current from node 1, $i_{01} = \sum_{\alpha=1}^{p_1} i_{\alpha,1}$; from node 2, $i_{02} = \sum_{\alpha=1}^{p_2} i_{\alpha,2}$ and so on. The expressions, $\sum i(t) = \sum_{\alpha=1}^{p_\beta} \sum_{\beta=1}^{k} i_{\alpha,\beta}(t)$, $\frac{di_{1,1}}{dt} = \frac{v_{L_{1,1}}}{L_{1,1}}$, $\frac{di_{01}}{dt} = \sum_{\alpha=1}^{p_1} \frac{v_{L_{\alpha,1}}}{L_{\alpha,1}}$ and their extensions are used interchangeably in the analysis of generalised k node, p bus system ahead. If the fault takes place at source/load line at node i, bus j ($SL_{j,i}$), then the fault location is evaluated using the effective faulty circuit as shown in Fig. 11(b). Here the location is calculated using buses related to $SL_{1,1}$ and $SL_{j,i}$. $r_{j,i}D_{j,i}$ and $l_{j,i}D_{j,i}$ give the equivalent resistance and inductance from bus j to node i whereas $r_{n,m}D_{n,m}$ and $l_{n,m}D_{n,m}$ give the equivalent resistance and inductance from bus n to node m. Using KVL for a PTP fault at bus j of node i from bus 1 of node 1, (19) and (20) are obtained.

$$2r_{1,1}D_{1,1}i_{1,1}(t) + 2\sum_{\beta=1}^{i-1} M_\beta r_{M_\beta} \sum_{\varepsilon=1}^{\beta} i_{0\varepsilon}$$

$$+ 2(D_{j,i} - x)r_{j,i} \sum_{\substack{(\alpha,\beta)=(1,1)\\(\alpha,\beta)\neq(j,i)}}^{p_\beta,k} i_{\alpha,\beta}(t)$$

$$+ R_f \sum i(t) + l_{1,1}D_{1,1}\frac{v_{L_{1,1}}(t)}{L_{1,1}}$$

$$+ \sum_{\beta=1}^{i-1} l_{M_\beta} M_\beta \sum_{(\alpha,\varepsilon)=(1,1)}^{p_{i-1},\beta} \frac{v_{L_{\alpha,\varepsilon}}(t)}{L_{\alpha,\varepsilon}}$$

$$+ (D_{j,i} - x)l_{j,i} \sum_{\substack{(\alpha,\beta)=(1,1)\\(\alpha,\beta)\neq(j,i)}}^{p_\beta,k} \frac{v_{L_{\alpha,\beta}}(t)}{L_{\alpha,\beta}} = u_{1,1}(t) \qquad (19)$$

$$2r_{j,i}xi_{j,i}(t) + l_{j,i}x\frac{v_{L_{j,i}}}{L_{j,i}} + R_f \sum i(t) = u_{j,i}(t) \qquad (20)$$

Similarly, as explained in previous subsections, rearranging (19) and (20) give the generalised fault distance expression from bus m of node n as given in (18a), which completes the proof. $\quad\square$

Further, the equivalent fault distance using all available terminal measurements can be defined as (21).

$$x|_{SL_{j,i}} = \frac{1}{pk} \sum_{\substack{\alpha=1\\(\alpha,\beta)\neq(j,i)}}^{p} \sum_{\beta=1}^{k} x|_{B_\alpha,N_\beta} \qquad (21)$$

Reliability conditions are defined as (22a) and (22b). Here (22a) suggests that fault locations calculated using different terminal buses are close to each other in magnitude. Equation (22b) suggests that each calculated fault location is lesser than the total line length, $D_{j,i}$.

$$\sum_{\substack{\alpha=2\\(\alpha,\beta)\neq(j,i)}}^{p} \sum_{\beta=2}^{k} x|_{B_\alpha,N_\beta} - \sum_{\substack{\alpha=1\\(\alpha,\beta)\neq(j,i)}}^{p} \sum_{\beta=1}^{k} x|_{B_\alpha,N_\beta} < D_{threh}$$
$$(22a)$$

$$\boldsymbol{x} \leq D_{j,i} : \boldsymbol{x} \in \left\{ \sum_{\substack{\alpha=1\\(\alpha,\beta)\neq(j,i)}}^{p} \sum_{\beta=1}^{k} x|_{B_\alpha,N_\beta} \right\} \qquad (22b)$$

D_{thresh} is a static threshold for practical implementation of (22a). The lower limit of setting D_{thresh} is restricted by the time to locate the fault. For faults with lower fault resistance, the response damps slowly. As a result of which, it is possible that a very low threshold does not satisfy (22a) until the response is absolutely damped. This can delay the time to locate the fault. Additionally, a high value of D_{thresh} may compromise the accuracy of fault location. A nominal value of around $\pm 5\% - 8\%$ can be selected as the static threshold for D_{thresh}. Throughout the study, the calculated fault distance for a fault at $SL_{j,i}$ is noticed to be composed of (a) $[u_{j,i}(t) - u_{n,m}(t)]$, (b) contribution of resistive and inductive component of $SL_{n,m}$, (c) contribution of resistive and inductive component of all *ILs* between $SL_{n,m}$ and $SL_{j,i}$, and (d) numerator and denominator contributions of resistive and inductive component of $SL_{j,i}$.

APPENDIX B
GENERALITY FOR FAULT LOCATION AT IL_{i-1}

Proof: If the fault takes place at the interconnecting line between nodes *i-1* and *i*, then the fault location is evaluated

using the effective faulty circuit as shown in Fig. 11(c). Using KVL for a PTP fault at IL_{i-1} with bus 1 of node 1 and bus j of node i, (23) and (24) are obtained respectively.

$$2r_{1,1}D_{1,1}i_{1,1}(t) + 2\sum_{\beta=1}^{i-2} M_\beta r_{M_\beta} \sum_{\varepsilon=1}^{\beta} i_{0\varepsilon}$$

$$+ 2(M_{i-1}-x)r_{M_{i-1}}\sum_{\varepsilon=1}^{i-1} i_{0\varepsilon}(t)$$

$$+ R_f \sum i(t) + l_{1,1}D_{1,1}\frac{v_{L_{1,1}}}{L_{1,1}}$$

$$+ \sum_{\beta=1}^{i-2} l_{M_\beta} M_\beta \sum_{(\alpha,\varepsilon)=(1,1)}^{p_\beta,\beta} \frac{v_{L_{\alpha,\beta}}}{L_{\alpha,\beta}} + (M_{i-1}-x)l_{M_{i-1}}$$

$$\sum_{(\alpha,\beta)=(1,1)}^{p_\beta,i-1} \frac{v_{L_{\alpha,\beta}}}{L_{\alpha,\beta}} = u_{1,1}(t) \tag{23}$$

$$2r_{j,i}D_{j,i}i_{j,i}(t) + 2xr_{M_{i-1}}\sum_{\varepsilon=i}^{k} i_{0\varepsilon}(t)$$

$$+ R_f \sum i(t) + l_{j,i}D_{j,i}\frac{v_{L_{j,i}}}{L_{j,i}}$$

$$+ xl_{M_{i-1}} \sum_{(\alpha,\beta)=(1,i)}^{p_\beta,k} \frac{v_{L_{\alpha,\beta}}}{L_{\alpha,\beta}} = u_{j,i}(t) \tag{24}$$

Rearranging (23) and (24) give the generalized fault location expression from bus m of node n as given in (18b). This completes the proof of Theorem 2. □

The equivalent fault distance and the reliability conditions can be worked out similarly to (21) and (22). Similar to the case of fault at $SL_{j,i}$, throughout the study, the calculated fault distance for a fault at IL_{i-1} is noticed to be composed of (a) $[u_{j,i}(t) - u_{n,m}(t)]$, (b) contribution of resistive and inductive component of $SL_{n,m}$, (c) contribution of resistive and inductive component of all ILs between $SL_{n,m}$ and IL_{i-1}, (d) contributions of resistive and inductive component of $SL_{j,i}$, and (e) numerator and denominator contributions of resistive and inductive component of IL_{i-1}.

REFERENCES

[1] V. Nougain, S. Mishra, and S. S. Jena, "Resilient protection of medium voltage DC microgrids against cyber intrusion," *IEEE Trans. Power Del.*, vol. 37, no. 2, pp. 960–971, Apr. 2022, doi: 10.1109/TP-WRD.2021.3074879.

[2] N. Doerry, J. Amy, and C. Krolick, "History and the status of electric ship propulsion, integrated power systems, and future trends in the U. S. Navy," *Proc. IEEE*, vol. 103, no. 12, pp. 2243–2251, Dec. 2015, doi: 10.1109/JPROC.2015.2494159.

[3] J. D. Herbst, A. L. Gattozzi, A. Ouroua, and F. M. Uriarte, "Flexible test bed for MVDC and HFAC electric ship power system architectures for Navy ships," in *Proc. IEEE Electric Ship Technol. Symp.*, 2011, pp. 66–71, doi: 10.1109/ESTS.2011.5770843.

[4] Z. Jin, L. Meng, J. M. Guerrero, and R. Han, "Hierarchical control design for a shipboard power system with DC distribution and energy storage aboard future more-electric ships," *IEEE Trans. Ind. Inform.*, vol. 14, no. 2, pp. 703–714, Feb. 2018, doi: 10.1109/TII.2017.2772343.

[5] K. Satpathi, A. Ukil, S. S. Nag, J. Pou, and M. A. Zagrodnik, "DC marine power system: Transient behavior and fault management aspects," *IEEE Trans. Ind. Inform.*, vol. 15, no. 4, pp. 1911–1925, Apr. 2019, doi: 10.1109/TII.2018.2864598.

[6] C. Yuan, M. A. Haj-ahmed, and M. S. Illindala, "Protection strategies for medium-voltage direct-current microgrid at a remote area mine site," *IEEE Trans. Ind. Appl.*, vol. 51, no. 4, pp. 2846–2853, Jul./Aug. 2015, doi: 10.1109/TIA.2015.2391441.

[7] V. Nougain, S. Mishra, and A. K. Pradhan, "MVDC microgrid protection using a centralized communication with a localized backup scheme of adaptive parameters," *IEEE Trans. Power Del.*, vol. 34, no. 3, pp. 869–878, Jun. 2019, doi: 10.1109/TPWRD.2019.2899768.

[8] R. M. Cuzner and V. Singh, "Future shipboard MVdc system protection requirements and solid-state protective device topological tradeoffs," *IEEE J. Emerg. Sel. Topics Power Electron.*, vol. 5, no. 1, pp. 244–259, Mar. 2017, doi: 10.1109/JESTPE.2016.2638921.

[9] S. Jiang, C. Fan, N. Huang, Y. Zhu, and M. He, "A fault location method for DC lines connected with DAB terminal in power electronic transformer," *IEEE Trans. Power Del.*, vol. 34, no. 1, pp. 301–311, Feb. 2019, doi: 10.1109/TPWRD.2018.2867851.

[10] W. Liu, F. Liu, X. Zha, M. Huang, C. Chen, and Y. Zhuang, "An improved SSCB combining fault interruption and fault location functions for DC line short-circuit fault protection," *IEEE Trans. Power Del.*, vol. 34, no. 3, pp. 858–868, Jun. 2019, doi: 10.1109/TPWRD.2018.2882497.

[11] A. Makkieh, V. Psaras, R. Peña-Alzola, D. Tzelepis, A. A. S. Emhemed, and G. M. Burt, "Fault location in DC microgrids based on a multiple capacitive earthing scheme," *IEEE J. Emerg. Sel. Topics Power Electron.*, vol. 9, no. 3, pp. 2550–2559, Jun. 2021, doi: 10.1109/JESTPE.2020.2995946.

[12] D. Wang, V. Psaras, A. A. S. Emhemed, and G. M. Burt, "A novel fault let-through energy based fault location for LVDC distribution networks," *IEEE Trans. Power Del.*, vol. 36, no. 2, pp. 966–974, Apr. 2021, doi: 10.1109/TPWRD.2020.2998409.

[13] Y. Yang, C. Huang, and Q. Xu, "A fault location method suitable for low-voltage DC line," *IEEE Trans. Power Del.*, vol. 35, no. 1, pp. 194–204, Feb. 2020, doi: 10.1109/TPWRD.2019.2930622.

[14] J. Park, J. Candelaria, L. Ma, and K. Dunn, "DC ring-bus microgrid fault protection and identification of fault location," *IEEE Trans. Power Del.*, vol. 28, no. 4, pp. 2574–2584, Oct. 2013, doi: 10.1109/TP-WRD.2013.2267750.

[15] R. Mohanty, U. S. M. Balaji, and A. K. Pradhan, "An accurate noniterative fault-location technique for low-voltage DC microgrid," *IEEE Trans. Power Del.*, vol. 31, no. 2, pp. 475–481, Apr. 2016, doi: 10.1109/TP-WRD.2015.2456934.

[16] V. Nougain, V. Nougain, and S. Mishra, "Low-voltage DC ring-bus microgrid protection with rolling mean technique," in *Proc. IEEMA Engineer Infinite Conf. (eTechNxT)*, 2018, pp. 1–6.

[17] J. Yang, J. E. Fletcher, and J. O'Reilly, "Short-circuit and ground fault analyses and location in VSC-Based DC network cables," *IEEE Trans. Ind. Electron.*, vol. 59, no. 10, pp. 3827–3837, Oct. 2012, doi: 10.1109/TIE.2011.2162712.

[18] C. Li, C. Zhao, J. Xu, Y. Ji, F. Zhang, and T. An, "A pole-to-pole short-circuit fault current calculation method for DC grids," *IEEE Trans. Power Syst.*, vol. 32, no. 6, pp. 4943–4953, Nov. 2017.

[19] J. Xu, S. Zhu, C. Li, and C. Zhao, "The enhanced DC fault current calculation method of MMC-HVDC grid with FCLs," *IEEE J. Emerg. Sel. Topics Power Electron.*, vol. 7, no. 3, pp. 1758–1767, Sep. 2019.

[20] J. Xu, Y. Lü, C. Zhao, and J. Liang, "A model-based DC fault location scheme for multi-terminal MMC-HVDC systems using a simplified transmission line representation," *IEEE Trans. Power Del.*, vol. 35, no. 1, pp. 386–395, Feb. 2020.

[21] O. M. K. K. Nanayakkara, A. D. Rajapakse, and R. Wachal, "Location of DC line faults in conventional HVDC systems with segments of cables and overhead lines using terminal measurements," *IEEE Trans. Power Del.*, vol. 27, no. 1, pp. 279–288, Jan. 2012.

[22] P. T. Lewis, B. M. Grainger, H. A. Al Hassan, A. Barchowsky, and G. F. Reed, "Fault section identification protection algorithm for modular multilevel converter-based high voltage DC with a hybrid transmission corridor," *IEEE Trans. Ind. Electron.*, vol. 63, no. 9, pp. 5652–5662, Sep. 2016.

[23] D. Tzelepis, G. Fusiek, A. Dyśko, P. Niewczas, C. Booth, and X. Dong, "Novel fault location in MTDC grids with non-homogeneous transmission lines utilizing distributed current sensing technology," *IEEE Trans. Smart Grid*, vol. 9, no. 5, pp. 5432–5443, Sep. 2018, doi: 10.1109/TSG.2017.2764025.

[24] H. Panahi, M. Sanaye-Pasand, R. Zamani, and H. Mehrjerdi, "A novel DC transmission system fault location technique for offshore renewable energy harvesting," *IEEE Trans. Power Del.*, vol. 35, no. 6, pp. 2885–2895, Dec. 2020, doi: 10.1109/TPWRD.2020.3010160.

[25] *International Organization for Standardization*, Standard ISO/IEC Guide 98-3:2008, ISO, Geneva, Switzerland, Sep. 10, 2007. [Online]. Available: https://www.iso.org/standard/50461.html

Vaibhav Nougain received the B.Tech degree in electrical engineering from Delhi Technological University (Formerly Delhi College of Engineering), New Delhi, India, in 2017 and the Ph.D. degree in electrical engineering from Indian Institute of Technology Delhi, New Delhi, in 2022. He was a Visiting Student with The Center for Electric Power and Energy, Technical University of Denmark, Kongens Lyngby, Denmark, in 2019. Since 2023, he has been working as a Postdoc Researcher with TU Delft, Delft, Netherlands, Faculty of Electrical Engineering, Mathematics, and Computer Science, the Group Intelligent Electrical Power Grids. His research interests include the protection and control of power electronics interfaced power systems.

Sukumar Mishra (Senior Member, IEEE) received the M.Tech and Ph.D. degrees in electrical engineering from the National Institute of Technology, Rourkela, India, in 1992 and 2000 respectively. He is currently a Professor with the Indian Institute of Technology Delhi, New Delhi, India, and has been its part for the past 17 years. He was the recipient of many accolades such as the INSA Medal for Young Scientist (2002), the INAE Young Engineer Award (2009, 2002), the INAE Silver Jubilee Young Engineer Award (2012), Samanta Chandra Shekhar Award (2016), IETE Bimal Bose award (2019), National Mission Innovation Champion award (2019), and NASI-Reliance Industries Platinum Jubilee Award for Application Oriented Innovation in Physical Sciences (2019). He has been granted Fellowships from academies like NASI (India), INAE (India), and professional societies like IET (U.K.), IETE (India), and IE (India). He has also been recognized as the INAE Industry Academic Distinguished Professor. His research interests include the fields of Power Systems, Power Quality Studies, Renewable Energy, and Smart Grid. Dr. Mishra is currently the ABB Chair Professor and was the NTPC, INAE, and Power Grid Chair Professor. He was also an Independent Director of the Cross Border Power Transmission Company Ltd. and the River Engineering Pvt. Ltd. He has carried out many important industrial consultations with TATA Power, Microtek, and others. Dr. Mishra has been working in close association with the IEEE Delhi Section Executive Committee for the past few years and is the Editor of IEEE TRANSACTIONS ON SMART GRID, IEEE TRANSACTIONS ON SUSTAINABLE ENERGY, and was an Area Editor for *IET Generation, Transmission & Distribution Journal*.

Soumya Shubhra Nag (Member, IEEE) received the B.E. degree from Jadavpur University, Kolkata, India, in 2009 and the M.Tech. and Ph.D. degrees from the Indian Institute of Technology (IIT) Kanpur, Kanpur, India, in 2011 and 2017, respectively, all in electrical engineering. From 2017 to 2018, he was a Research Fellow with the Rolls-Royce Corporate Laboratory, Nanyang Technological University, Singapore. He is currently an Assistant Professor with IIT Delhi, New Delhi, India. His research interests include power electronic converters for transportation electrification, DC distribution systems, and renewable energy systems.

Aleksandra Lekić (Senior Member, IEEE) received the B.Sc, M.Sc, and Ph.D. degrees in electrical engineering from the School of Electrical Engineering, University of Belgrade, Belgrade, Serbia, in 2012, 2013, and 2017, respectively. Between 2012 and 2018, she was a Teaching Assistant with the School of Electrical Engineering, University of Belgrade and an Assistant Professor from 2018 to 2019. In 2019, she was a Postdoctoral Researcher with the Department of Electrical Engineering (ESAT), KU Leuven, Leuven, Belgium and Institute EnergyVille, Genk, Belgium. Since January 2020, she is a tenured Assistant Professor with Faculty of Electrical Engineering, Mathematics and Computer Science, the Group Intelligent Electrical Power Grids, TU Delft, Delft, Netherlands. Dr. Lekić leads a team of researchers specializing in the Control of HVDC/AC power systems. She is an Associate Editor for *International Journal of Electrical Power & Energy Systems, Elsevier*. Dr. Lekić represents TU Delft in the General Assembly in the CRESYM organization, committed to open-source software development for the electrical grids.